LITHIUM EXTRACTION

Solar transpiration–powered lithium extraction and storage

Yan Song[1]†, Shiqi Fang[1]†, Ning Xu[1], Monong Wang[2], Shuying Chen[1], Jun Chen[3,4], Baoxia Mi[2]*, Jia Zhu[1,3]*

Lithium mining is energy intensive and environmentally costly. This is because lithium ions are typically present in brines as a minor component mixed with physiochemically similar cations that are difficult to separate. Inspired by nature's ability to selectively extract species in transpiration, we report a solar transpiration–powered lithium extraction and storage (STLES) device that can extract and store lithium from brines using natural sunlight. Specifically, the device uses a hierarchically structured solar transpirational evaporator to create a pressure gradient, which allows for the extraction of lithium from brines through a membrane and its storage in a vascular storage layer. Long-term experiments, various membrane tests, and different size assessments demonstrate the stability, compatibility, and scalability of STLES. This solar-powered mining technology provides an alternative developing pathway toward the sustainable extraction of critical resources.

With the increasing demand for lithium in renewable technologies (*1*), it is imperative that lithium extraction be environmentally and socially responsible to ensure a sustainable future (*2*–*4*). Currently, lithium is sourced mainly from hard-rock ores through thermochemical routes or from brines through an evaporative process (*5*, *6*). The evaporitic method, being used in 87% of lithium mining facilities, has limited kinetics, has intensive water usage, and is suitable for high-grade brines only (*7*). Sustainable technologies for extracting lithium from various brines are critical to ensure a clean and reliable lithium supply (*8*–*11*).

In nature, many living systems have evolved to efficiently extract specific species. Particularly, halophytes—plants that thrive in saline habits—have developed an extraction-storage-release (ESR) mechanism to take up nutrients from high-salinity soil or waters without being harmed (*12*). They exploit transpiration to extract nutrients like other plants (*13*), but they also have specialized organs to store and discharge excess salts from their body. This additional salt storage and release mechanism is critical for halophytes' survival in saline, without which they would perish because of drought (*14*).

With this inspiration, we developed a solar transpiration–powered lithium extraction and storage (STLES) device, with the goal of greener lithium mining. Its structure and working principle are presented in Fig. 1, A to E. Our strategy captures the main attributes of the ESR mechanism in halophytes and involves three main steps: (i) Solar transpiration creates a high capillary pressure within the evaporator; (ii) this transpiration pressure is transmitted to the membrane, resulting in an influx of lithium from the brine to the lithium storage layer; and (iii) water circulation transports the extracted lithium to the reservoir and regenerates the device.

To achieve efficient and stable solar transpiration–powered lithium extraction, a stringent set of requirements must be satisfied. First, the passively generated transpiration pressure P_{trans} within the evaporator by capillarity must exceed the operating pressure of nanofiltration (NF). The Young-Laplace equation (*15*) predicts that $P_{trans} = 4\gamma\cos\theta/d_p$, where γ is the surface tension of water, θ is the contact angle of water on the evaporator, and d_p is the pore diameter of the evaporator (Fig. 1F and supplementary text, section 1). Considering that NF typically runs at 5 to 20 bar (*16*), the transpirational evaporator must be hydrophilic ($\theta \sim 60°$) and nanoporous ($d_p < 288$ nm). Second, the evaporator must generate high transpiration flux to enable high lithium productivity. Theoretical analysis shows that transpiration flux J is slightly dependent on θ and d_p, but it is predominantly governed by the temperature of the evaporator T_{evap} (Fig. 1G and supplementary text, section 2). A 30-fold increase in flux (0.05 to 1.45 liter m^{-2} $hour^{-1}$) is observed as T_{evap} increases from 300 to 350 K. In this regard, an interfacial solar-driven evaporator is ideal because it can harness solar energy to accelerate transpiration with a high solar-to-thermal conversion efficiency (>90%) (*17*–*23*). Finally, the lithium storage layer must be able to resist cavitation and salt deposits for stable lithium extraction (fig. S1) (*24*). Tight channels that are smaller than the critical size of bubble nuclei ($D_C \approx 4\gamma/P_{trans}$) are required to prevent bubble-induced cavitation (blue region in Fig. 1H and supplementary text, section 3), and high porosity is necessary to accommodate the extracted salts.

We develop a passive, floating STLES (Fig. 1A) that consists of an aluminum-based hierarchical membrane as the high-pressure (18 bar), high-flux (1.8 liter m^{-2} $hour^{-1}$) solar transpirational evaporator (Fig. 1C); a size-controllable fused-silica frit as the lithium storage layer (Fig. 1D); and a NF membrane (Fig. 1E). The STLES can extract and store lithium from brines using natural sunlight, requiring no arable land or additional energy input.

Solar transpirational evaporator

As an example of demonstration, we apply aluminum nanoparticles (Al NPs)–decorated anodic aluminum oxide (AAO) as the solar transpirational evaporator, which can be replaced by less-expensive materials, such as hydrogel membranes (*25*) and resin-based cellular fluidics (*26*). The nanometer-sized matrix is important to generate high transpiration pressure. Cross-sectional scanning electron microscope (SEM) (Fig. 1C) shows that the evaporator has a highly porous matrix (surface porosity $\varepsilon = 0.5$) with an average pore diameter of 100 nm, which gives rise to a theoretical P_{trans} of 18.5 bar ($\theta = 50°$). P_{trans} is further determined experimentally by interfacing the evaporator with osmosis and observing the magnitude of corresponding water flux J_w (figs. S5 and S6 and supplementary text, section 4) (*27*). According to the solution-diffusion model, $J_w = A(P_{trans} - \Pi)$, where A is the water permeability coefficient and Π is the osmotic pressure (*28*, *29*). Particularly, $J_w = 0$ when $P_{trans} = \Pi$. The zero-water flux point in Fig. 2A suggests that our evaporator has a practical P_{trans} of 18.7 bar. This value is in good agreement with the theoretical P_{trans} (18.5 bar) and is sufficient to drive NF (*16*).

The hierarchical structure is essential for achieving high-flux transpiration using solar energy. As shown in Fig. 1C and fig. S7, it consists of randomly distributed, different-sized Al NPs (5 to 60 nm), Al film (~100 nm), and nanoporous AAO matrix. This hybrid structure enables efficient and localized photothermal heating, owing to coupling-enhanced broadband absorption and strong nonradiative plasmon decay (*30*, *31*). As a result, compared with a conventional nonphotothermal evaporator (*32*), our solar transpirational evaporator exhibits enhanced solar absorptance (97% versus 11%; fig. S8), higher temperature (354 versus 320 K under one-sun irradiation; Fig. 2B), and improved transpiration flux (1.28 versus 0.59 liter m^{-1} $hour^{-1}$ under one-sun irradiation; Fig. 2C).

[1]National Laboratory of Solid State Microstructures, College of Engineering and Applied Sciences, Jiangsu Key Laboratory of Artificial Functional Materials, Collaborative Innovation Center of Advanced Microstructures, Frontiers Science Center for Critical Earth Material Cycling, Nanjing University, Nanjing 210093, China. [2]Department of Civil and Environmental Engineering, University of California, Berkeley, Berkeley, CA 94720, USA. [3]School of Sustainable Energy and Resources, Nanjing University, Suzhou 215163, China. [4]School of Earth Sciences and Engineering, Nanjing University, Nanjing 210093, China.
***Corresponding author. Email: mib@berkeley.edu (B.M.); jiazhu@nju.edu.cn (J.Z.)**
†These authors contributed equally to this work.

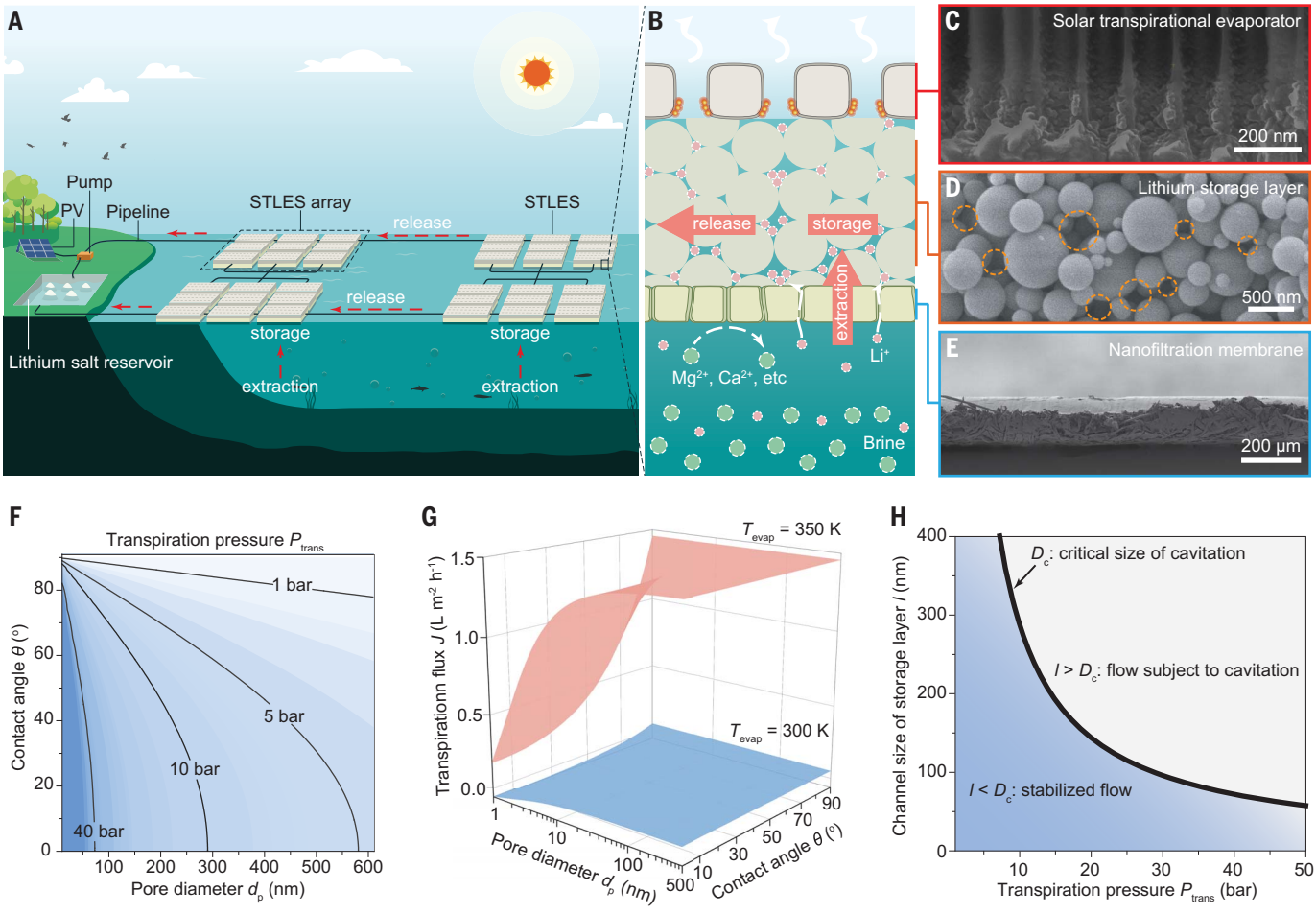

Fig. 1. Concept and design of STLES. (**A**) STLES can float and extract lithium from brines at scale using only ambient sunlight as the source of energy. PV, photovoltaic array. (**B**) The operating principle of STLES involves solar-driven transpiration, which creates a high capillary pressure within the evaporator. This pressure is then transmitted to the NF membrane, causing an influx of lithium from the brine to the storage layer. Water circulation transports the extracted lithium to the reservoir and regenerates the STLES. (**C** to **E**) Cross-sectional SEM images of the three critical components of STLES [same view direction as (B)]. From top to bottom, solar transpirational evaporator (C), lithium storage layer (D), and NF membrane (E). Circles in (D) indicate the water flow channels. (**F**) Transpiration pressure P_{trans} as a function of contact angle θ and pore diameter d_p. (**G**) Transpiration flux J as a function of T_{evap}, θ, and d_p. Larger J can be achieved by increasing θ, d_p, and particularly T_{evap}. (**H**) Critical nucleus size of cavitation versus P_{trans}. l is the channel size of the storage layer. When $l < D_C$ (blue region), nucleated bubble is suppressed by geometrical confinement, and thus no cavitation inception occurs.

Lithium storage layer

The lithium storage layer in STLES is essential for (i) the delivery of water and pressure between the evaporator and membrane, (ii) mechanical support, and (iii) storage of extracted lithium salts. To ensure stable lithium extraction, the storage layer needs to resist both cavitation and embolism. On one hand, transpiration-induced tension places the storage layer's water in a metastable state, making it vulnerable to cavitation, which blocks water transport locally with a vapor phase embolus (*25*). On the other hand, the extracted salts may accumulate in the storage layer or on the evaporator, which can slow down or even impede transpiration (fig. S1).

We use a ceramic frit as the lithium storage layer. It consists of uniform and percolative channels and is synthesized by fusing monodisperse silica microspheres together through spark plasma sintering (Fig. 2D). This microsphere-based lithium storage layer has four distinctive characteristics. First, its channel size l is exclusively determined by the diameter of precursor spheres ($l \approx d_{sphere}/4$) and can be finely controlled from nanometers to micrometers through proper selection of d_{sphere}. We choose silica spheres with d_{sphere} = 700 nm as the precursor (Fig. 2E), expecting l = 150 nm. Mercury intrusion porosimetry confirms that the fabricated storage layer has a void size of 151 nm (Fig. 2F), smaller than D_C (160 nm for P_{trans} = 18.5 bar), thereby effectively reducing the cavitation risk. Second, it consists of an interconnected network of pores (Fig. 1D) that allow for percolative water pathways to prevent embolism (*33*). That is, even if extracted salts block some water paths, water transport can continue uninterrupted through adjacent unembolized paths (fig. S9). Third, the storage layer, with a porosity of ~45% and a pore size of 151 nm, is sufficient for hosting extracted salts (supplementary text, section 5). Fourth, the storage layer, made of fused silica ceramic, has weak interactions with salts, allowing for easy regeneration through water rinse (fig. S10).

To confirm the stable water flow in STLES, a transpiration test was conducted continuously under 500– and 1000–W m^{-2} irradiations for 50 hours, representing cloudy and sunny days, respectively. During the 50-hour transpiration tests, no obvious degradation in transpiration fluxes was observed, which suggests excellent working stability (Fig. 2G).

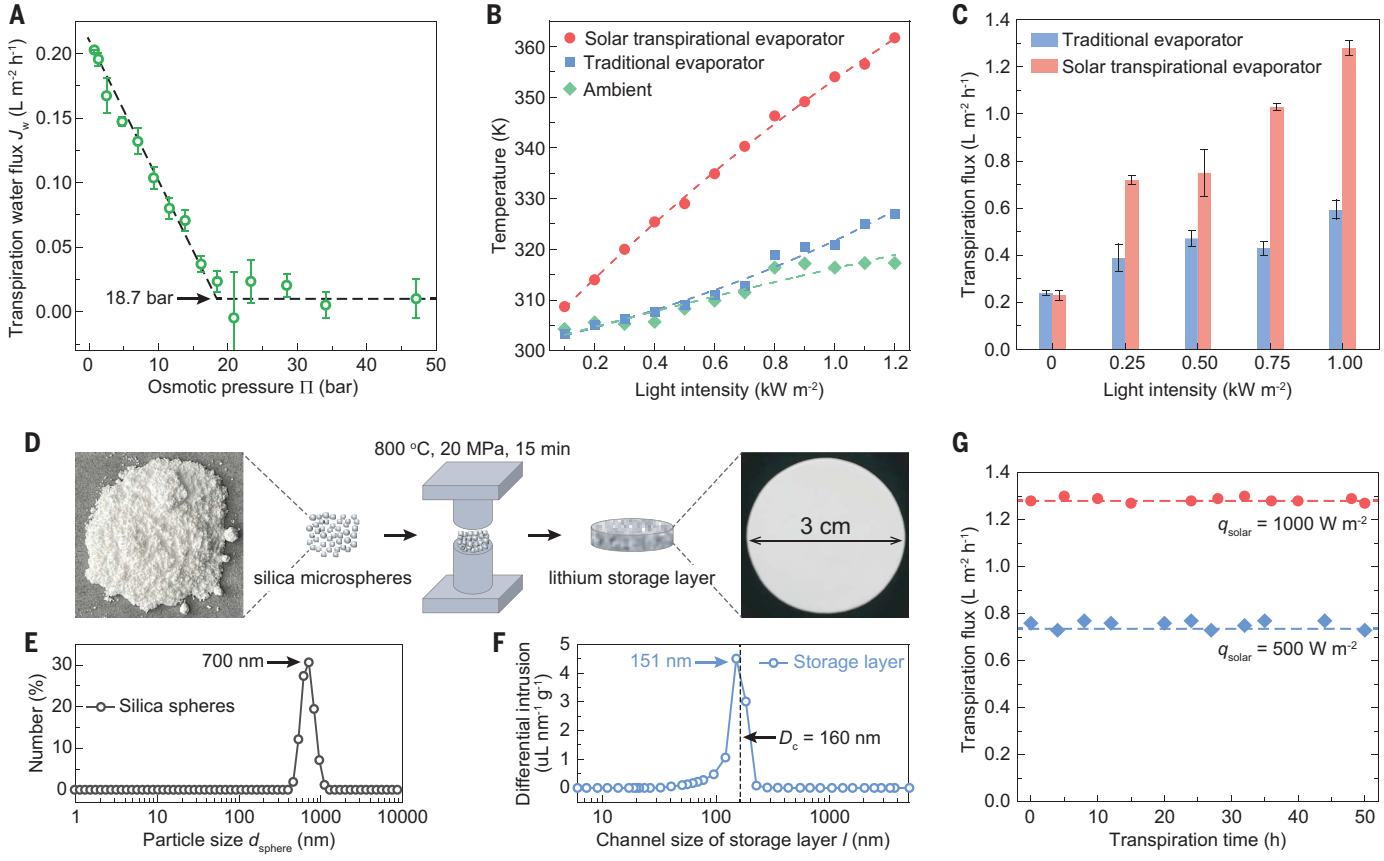

Fig. 2. Design and characterization of solar transpirational evaporator and lithium storage layer. (**A**) Water flux J_w driven by transpiration as a function of osmotic pressure Π. The practical P_{trans} is determined from the zero-flux point and is 18.7 bar. Π is calculated using OLI Stream Analyzer 3.1 and is listed in table S1 (*44*). Error bars are the standard deviation of J_w over three repetitions. (**B**) Light-driven temperature of photothermal evaporator, traditional evaporator, and ambient. (**C**) Transpiration fluxes of photothermal and traditional evaporators under different solar irradiances. Error bars are the standard deviation of transpiration fluxes over three repetitions. (**D**) Schematic of the fabrication process of the lithium storage layer. Monodisperse silica microspheres are fused together through spark plasma sintering. (**E**) Particle size distribution of silica microspheres determined by dynamic light scattering. (**F**) Channel size distribution of lithium storage layer determined by mercury intrusion. The average channel size (151 nm) of the lithium storage layer is below D_C (160 nm), suggesting excellent ability to stabilize the thermodynamically metastable water flow. (**G**) Water fluxes by transpiration through the lithium storage layer over the course of 50 hours at 500 and 1000 W m^{-2}.

Device fabrication and lithium extraction performance

In light of the above designs, a proof-of-concept STLES platform (Fig. 3A) has been developed to demonstrate the feasibility of our approach. The platform comprises an array of modules (Fig. 3B and figs. S11 and S12), each with eight layers (Fig. 3C). Various types of brines have been examined because the performance of lithium extraction is substantially influenced by the brine chemistry, particularly the salinity and the mass ratio of Mg^{2+} to Li^+ (MLR) (*6*, *7*, *34*). The lithium extraction performance of STLES is assessed on the basis of two figures of merit: Li^+ permeance (i.e., how quickly Li^+ is extracted) and Li^+ selectivity (i.e., the degree to which Li^+ purity is enhanced).

Figure 3D shows the dependence of lithium extraction performance on the MLR of brines. Feed solutions are LiCl-$MgCl_2$ mixtures with a fixed salinity of 1.0 g liter^{-1} and varying MLRs (table S2). The apparently reduced Li^+ permeance at higher MLRs is due to the decrease of feed Li^+ concentration rather than the increase of MLR. This is evidenced in fig. S13, which shows that Li^+ permeance increases exponentially with the feed Li^+ concentration. Additionally, as the MLR of feed solutions increases, Li^+ selectivity (S_{Li}) also increases. This is because Li^+ rejection decreases from 70 to 26%, whereas Mg^{2+} rejection remains around 99% (fig. S14). The reduced rejection of Li^+ at higher MLRs is because of the stronger charge screening effect, which promotes the permeation of Cl^- and facilitates the transport of Li^+ (*35*).

To study the impact of feed salinity on lithium extraction, LiCl-$MgCl_2$ mixtures with a fixed MLR of 80 and varying salinities ranging from 0.2 to 20 g liter^{-1} are used as the feed solutions (table S3). Figure 3E shows that when increasing the feed salinity, lithium permeance increases first because salt partitioning into the membrane is enhanced at higher salinities, resulting in higher salt flux. This trend changes above 1.0 g liter^{-1}, and lithium permeance declines gradually with the feed salinity because greater osmotic pressure at higher salinity decreases the effective transmembrane pressure. Li^+ flux is maintained up to a salinity of 15 g liter^{-1} with an osmotic pressure of 10.7 bar (table S4). The progressively decreasing S_{Li} as feed salinity increases is attributable to the accumulation of Mg^{2+} near the membrane surface, which compromises the rejection of Mg^{2+} (*10*, *35*).

To further explore the feasibility of STLES, it was applied to diluted aged brines from China's three major salt lakes (*36*). These brines have a salinity of 1 g liter^{-1} and contain various ions, such as Li^+, Na^+, K^+, Mg^{2+}, Ca^{2+}, Cl^-, SO_4^{2-}, and others, which could greatly affect the extraction of lithium (*6*). Compositions of brines before and after transpiration-driven lithium

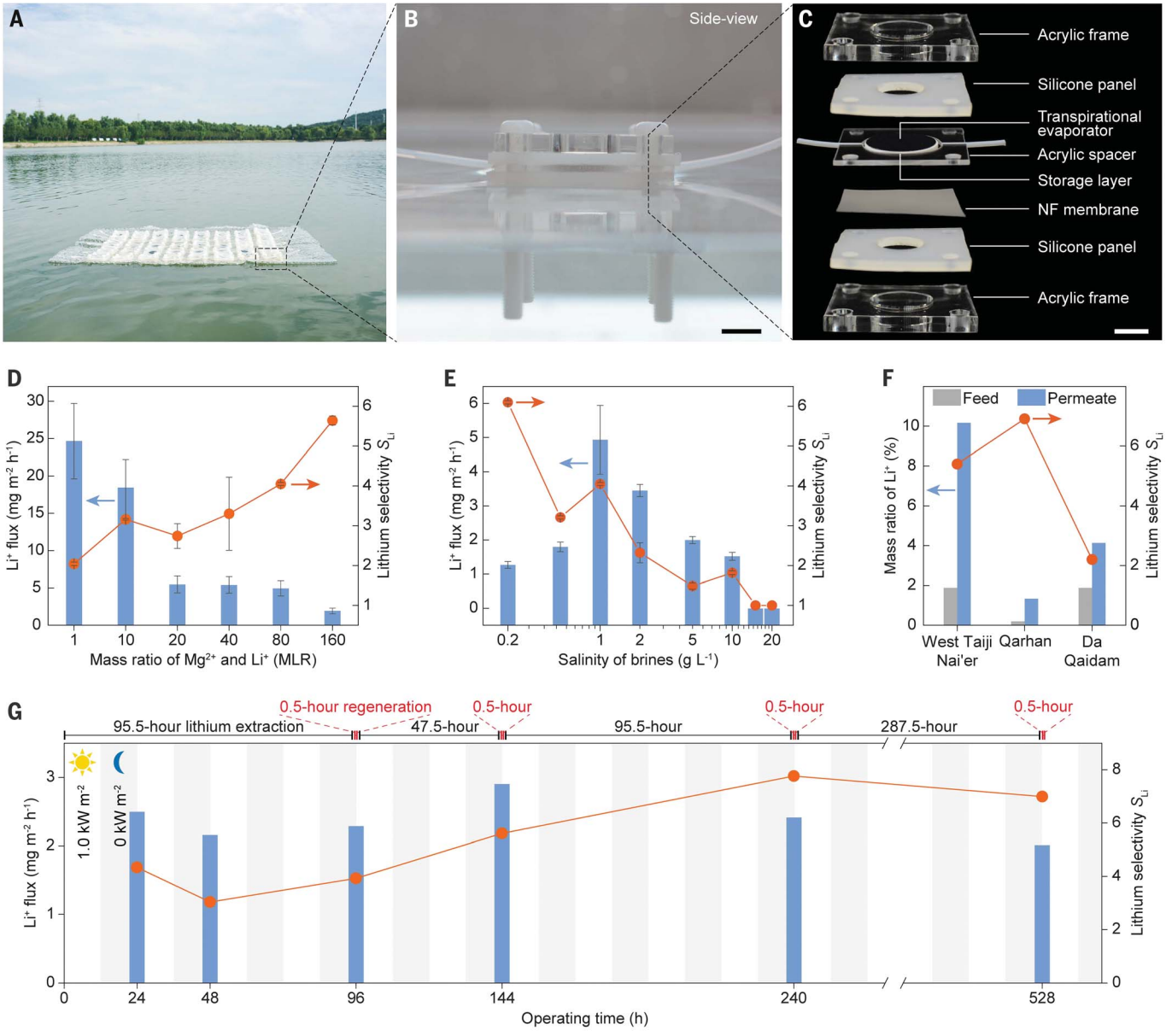

Fig. 3. Device fabrication and lithium extraction performance. (**A**) Standalone STLES array floats on water. (**B**) Side-view image of STLES. Scale bar, 1 cm. (**C**) Optical images of the eight layers of STLES. Scale bar, 1 cm. (**D**) Li^+ flux and Li^+ selectivity of STLES as a function of the MLR of brines. Feed solutions are LiCl-$MgCl_2$ mixtures with a fixed salinity of 1.0 g $liter^{-1}$ and varying MLRs. (**E**) Li^+ flux and Li^+ selectivity of STLES as a function of the salinity of brines. Feed solutions are LiCl-$MgCl_2$ mixtures with a fixed MLR of 80 and varying salinities. (**F**) (Left) Lithium content in the feed and permeate of STLES for aged brines from China's three major salt lakes. (Right) The corresponding lithium selectivity. (**G**) Stability test of STLES under simulated daily cycles, with 1.0–kW m^{-2} irradiation for 12 hours followed by 12 hours of darkness. Feed solution is a LiCl-$MgCl_2$ brine with a salinity of 1.0 g $liter^{-1}$ and a MLR of 80.

extraction are given in table S5. Figure 3F demonstrates that STLES can successfully extract lithium from brines, with the selectivity of extraction depending on the brine composition. Qarhan, which has the lowest Li^+ fraction in the feed, exhibits the highest S_{Li} of 7, which agrees with our findings in Fig. 3D. These results confirm the effectiveness of our approach in real brines. Additionally, selectivity can be further enhanced through membrane advancement, as explained in more detail below.

Similar to halophytes, a specific advantage of STLES is its operating stability under salty conditions because it has abundant pores to accommodate the extracted salts and can be regenerated through water circulation. To confirm these benefits, we assessed STLES's long-term lithium extraction performance in a brine with a salinity of 1.0 g $liter^{-1}$ and a MLR of 80 under simulated daily cycles, with 1.0–kW m^{-2} irradiation for 12 hours followed by 12 hours of darkness. STLES maintained both productivity and selectivity after 528 hours with only 2 hours of regeneration in total (Fig. 3G). The collection-regeneration process has negligible impact on productivity (<0.1%) because it occurs at night when the transpiration flux is lower and only requires a small portion of time (supplementary text, section 6).

Compatibility and scalability

This STLES design is showcased as a proof of concept and can be further enhanced by integrating advancements in the fields of solar evaporation (*18*), membrane (*37*), microfluidics

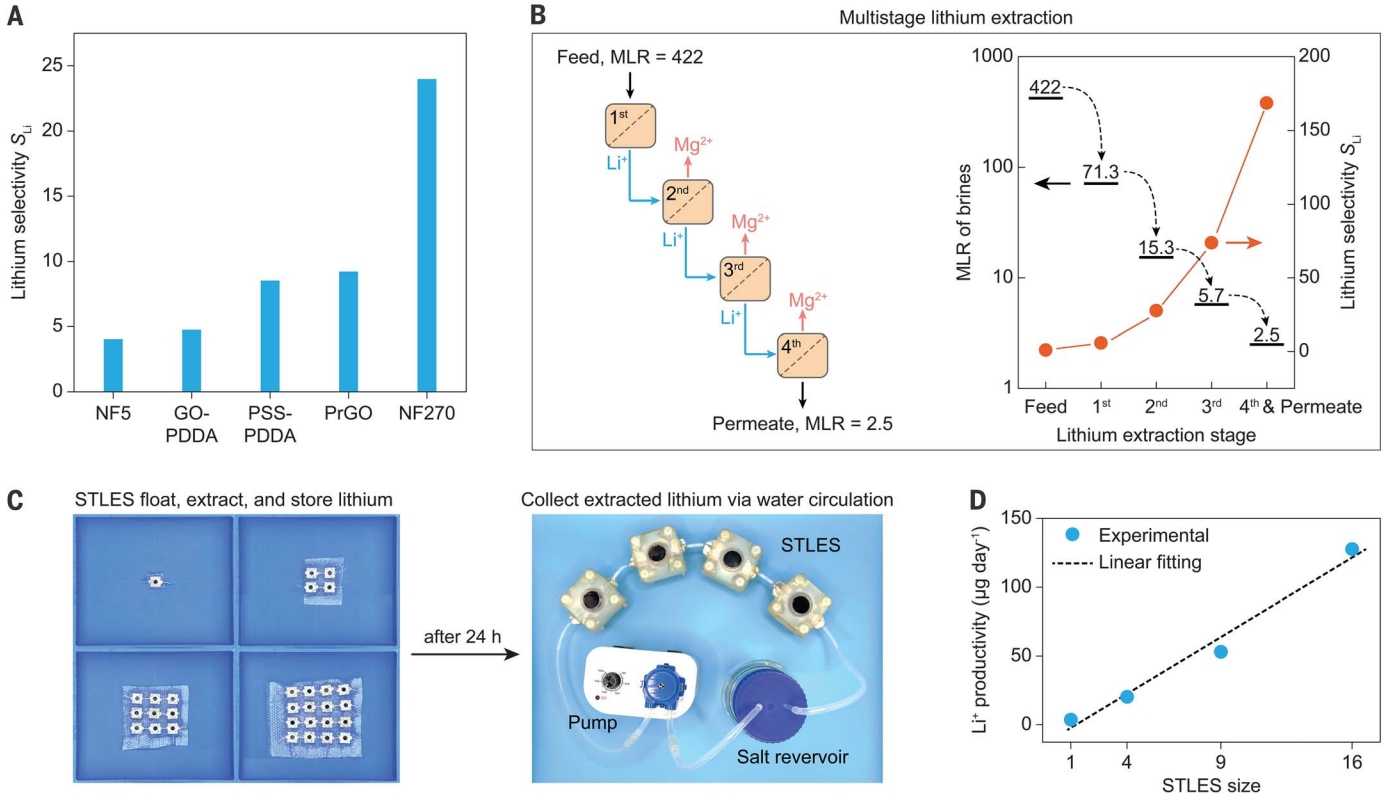

Fig. 4. Compatibility and scalability of STLES. (**A**) Lithium selectivity of STLES using different NF membranes. Feed solutions are a LiCl-$MgCl_2$ mixture with a salinity of 1.0 g liter^{-1} and a MLR of 80. (**B**) Multistage lithium extraction. (Left) Schematic of staged extraction. (Right) MLR of brines and the corresponding lithium selectivity as a function of the number of lithium extraction stages. (**C**) Setup used to characterize the outdoor lithium extraction performance of four STLES platforms containing 1, 4, 9, and 16 modules, respectively. (**D**) Lithium productivity of a STLES platform scales linearly with the number of modules used, demonstrating excellent scalability.

(*26*), and others. STLES is compatible with different types of membranes, which implies that its lithium extraction performance can benefit naturally from the advancement in membrane technology. To demonstrate this, we fabricate and test STLES using both laboratory-made and commercial NF membranes (see membrane details in the materials and methods). Figure 4A shows that STLES can work with various types of NF membranes, achieving lithium selectivity as high as 24. Additionally, transition-state theory reveals that STLES's selectivity is governed by the energy barrier difference presented by the NF membrane to Mg^{2+} and Li^+ transport (ΔE): $S_{Li} = \exp(\Delta E/k_B T)$, where k_B is Boltzmann's constant and T is the temperature (supplementary text, section 7). This suggests that the Li^+ selectivity in our approach can be improved by deliberate shaping of energy barriers for solute transport through the NF membrane. This can be achieved by modification of membrane charge (*38*, *39*), variation of pore size (*40*, *41*), and incorporation of specific chemical functionality (*42*, *43*).

In addition to material advancement, STLES's performance can also be enhanced through system design. As illustrated in Fig. 4B, multiple STLES are connected in series, where permeate from the previous stage becomes the feed for the next stage. We studied the feasibility and performance of this multistage lithium extraction system to treat a mixture of LiCl and $MgCl_2$ with a salinity of 1.0 g liter^{-1} and a MLR of 422. The MLR of the brine decreases with the number of lithium extraction stages (Fig. 4B, right). After four extraction stages, the MLR is reduced from 422 to 2.5, corresponding to $S_{Li} = 168$, which is about two orders of magnitude higher than that of a single stage ($S_{Li} = 2.3$ to 5.9; Fig. 3D). The superliner, exponential dependence of lithium selectivity on the number of stages suggests that the lithium extraction performance in our approach can be further improved with process engineering, such as multistage extraction (*9*).

The modular configuration enables the combination of multiple STLES to create a large platform that can extract lithium at scale. To demonstrate scalability, we tested four STLES platforms containing 1, 4, 9, and 16 modules, respectively (Fig. 4C, left). In the test, STLES are first placed on a LiCl-$MgCl_2$ brine with a salinity of 1.0 g liter^{-1} and a MLR of 80 to extract lithium. After 24 hours, STLES are taken out, and the extracted lithium salts are collected through water circulation (Fig. 4C, right). The stand-alone STLES is able to produce 33.2 mg_{Li} m^{-2} day^{-1} from 3-mg_{Li} liter^{-1} brine under ambient outdoor conditions—average solar irradiance, temperature, and relative humidity are 240 W m^{-2}, 28.9°C, and 65%, respectively (fig. S15). The lithium productivity of the STLES platform scales linearly with the number of modules adopted, which highlights the excellent scalability of our approach (Fig. 4D).

Conclusions

This work reports the design and demonstration of a STLES device that extracts lithium from brines at ambient conditions by using natural sunlight, requiring no arable land, and generating near-zero greenhouse gas. STLES presents several advantages over current and emerging lithium extraction approaches. First, once installed, its passive fashion allows for cost-, energy-, and carbon-effective lithium mining. Second, it can be seamlessly integrated with existing evaporation ponds, which are used in 87% of lithium mining facilities (*7*), lowering installed costs. Third, it can float on brines, reducing land footprints. Finally, it is expected that the use of a high–transpiration pressure evaporator [e.g., hydrogel membrane (*25*, *32*)] in STLES would facilitate the treatment of

hypersaline brines with osmotic pressures up to 400 bar, fivefold greater than the pressure limit of current membrane filtration systems.

REFERENCES AND NOTES

1. K. Hund, D. La Porta, T. P. Fabregas, T. Laing, J. Drexhage, "Minerals for Climate Action: The Mineral Intensity of the Clean Energy Transition" (World Bank Group, 2023).
2. R. Herrington, *Nat. Rev. Mater.* **6**, 456–458 (2021).
3. W. Liu, D. B. Agusdinata, *J. Clean. Prod.* **260**, 120838 (2020).
4. J. M. Turner, *Science* **376**, 1361 (2022).
5. A. Z. Haddad *et al*., *Nature* **616**, 245–248 (2023).
6. M. L. Vera, W. R. Torres, C. I. Galli, A. Chagnes, V. Flexer, *Nat. Rev. Earth Environ.* **4**, 149–165 (2023).
7. V. Flexer, C. F. Baspineiro, C. I. Galli, *Sci. Total Environ.* **639**, 1188–1204 (2018).
8. X. Chen *et al*., *Nat. Water* **1**, 808–817 (2023).
9. R. Wang, R. Alghanayem, S. Lin, *Environ. Sci. Technol.* **57**, 14464–14471 (2023).
10. R. Wang, R. He, T. He, M. Elimelech, S. Lin, *Nat. Water* **1**, 291–300 (2023).
11. O. A. Kazi *et al*., *Adv. Mater.* **35**, e2300913 (2023).
12. M.-N. Grigore, C. Toma, *Anatomical Adaptations of Halophytes: A Review of Classic Literature and Recent Findings* (Springer, 2017).
13. P. S. Nobel, *Physicochemical and Environmental Plant Physiology* (Academic Press, 1999).
14. D. Bartels, R. Sunkar, *Crit. Rev. Plant Sci.* **24**, 23–58 (2005).
15. P. G. de Gennes, *Rev. Mod. Phys.* **57**, 827–863 (1985).
16. P. Marchetti, M. F. Jimenez Solomon, G. Szekely, A. G. Livingston, *Chem. Rev.* **114**, 10735–10806 (2014).
17. P. Tao *et al*., *Nat. Energy* **3**, 1031–1041 (2018).
18. N. Xu *et al*., *Nat. Water* **1**, 494–501 (2023).
19. F. Zhao, Y. Guo, X. Zhou, W. Shi, G. Yu, *Nat. Rev. Mater.* **5**, 388–401 (2020).
20. C. Chen, Y. Kuang, L. Hu, *Joule* **3**, 683–718 (2019).
21. L. Zhou, X. Li, G. W. Ni, S. Zhu, J. Zhu, *Natl. Sci. Rev.* **6**, 562–578 (2019).
22. L. Zhang *et al*., *Energy Environ. Sci.* **14**, 1771–1793 (2021).
23. T. Ding, Y. Zhou, W. L. Ong, G. W. Ho, *Mater. Today* **42**, 178–191 (2021).
24. S. Zhang *et al*., *Nat. Commun.* **15**, 238 (2024).
25. T. D. Wheeler, A. D. Stroock, *Nature* **455**, 208–212 (2008).
26. N. A. Dudukovic *et al*., *Nature* **595**, 58–65 (2021).
27. T. Y. Cath, A. E. Childress, M. Elimelech, *J. Membr. Sci.* **281**, 70–87 (2006).
28. G. M. Geise, D. R. Paul, B. D. Freeman, *Prog. Polym. Sci.* **39**, 1–42 (2014).
29. M. Heiranian, H. Fan, L. Wang, X. Lu, M. Elimelech, *Chem. Soc. Rev.* **52**, 8455–8480 (2023).
30. L. Zhou *et al*., *Nat. Photonics* **10**, 393–398 (2016).
31. L. Zhou *et al*., *Sci. Adv.* **2**, e1501227 (2016).
32. Y. Wang, J. Lee, J. R. Werber, M. Elimelech, *Sci. Adv.* **6**, eaax5253 (2020).
33. M. Bouda *et al*., *Science* **378**, 642–646 (2022).
34. S. Xu *et al*., *J. Membr. Sci.* **635**, 119441 (2021).
35. R. He *et al*., *J. Membr. Sci.* **663**, 121027 (2022).
36. The term "aged brine" refers to salt lake water left after the production of sodium and potassium. It usually contains, in concentrated form, lithium and magnesium chlorides and sulfates, whereas the content of sodium and potassium is low.
37. R. Epsztein, R. M. DuChanois, C. L. Ritt, A. Noy, M. Elimelech, *Nat. Nanotechnol.* **15**, 426–436 (2020).
38. R. Epsztein, W. Cheng, E. Shaulsky, N. Dizge, M. Elimelech, *J. Membr. Sci.* **548**, 694–701 (2018).
39. W. Cheng *et al*., *J. Membr. Sci.* **559**, 98–106 (2018).
40. C. Boo *et al*., *Environ. Sci. Technol.* **52**, 7279–7288 (2018).
41. R. M. DuChanois, R. Epsztein, J. A. Trivedi, M. Elimelech, *J. Membr. Sci.* **581**, 413–420 (2019).
42. H. Farrokhzad, S. Darvishmanesh, G. Genduso, T. Van Gerven, B. Van der Bruggen, *Electrochim. Acta* **158**, 64–72 (2015).
43. M. Vaselbehagh, H. Karkhanechi, R. Takagi, H. Matsuyama, *J. Membr. Sci.* **490**, 301–310 (2015).
44. Analyzer 3.1 (OLI Systems Inc.).

ACKNOWLEDGMENTS

We thank S. Lin (Vanderbilt University) for valuable discussions; J. Liang, Y. Yang, W. Zhao, and Z. Wu (Nanjing University) for help with SEM tests; and X. Xu (Nanjing University) for help with cross-flow NF tests. We also acknowledge the microfabrication center of the National Laboratory of Solid State Microstructures (NLSSM) for their technical support. **Funding:** This work is jointly supported by the National Natural Science Foundation of China (51925204, 92262305, 52322211, 52102262, and 52003116), the National Key Research and Development Program of China (2022YFB3804902 and 2022YFA1404704), and the Carbon Peaking and Carbon Neutrality Science and Technology Innovation Fund of Jiangsu Province (BK20220035). This work has also been supported by the New Cornerstone Science Foundation through the XPLORER PRIZE. **Author contributions:** Conceptualization: Y.S., S.F., and J.Z. Methodology: Y.S., S.F., N.X., and M.W. Investigation: Y.S. and S.F. Visualization: Y.S., S.F., and S.C. Funding acquisition: Y.S., N.X., J.C., B.M., and J.Z. Project administration: Y.S., N.X., J.C., B.M., and J.Z. Supervision: Y.S., N.X., J.C., B.M., and J.Z. Writing – original draft: Y.S., S.F., N.X., S.C., J.C., and J.Z. Writing – review & editing: Y.S., S.F., N.X., M.W., S.C., J.C., B.M., and J.Z. **Competing interests:** Y.S., S.F., and J.Z. are inventors on a patent application related to this work filed by Nanjing University. The other authors declare that they have no competing interests. **Data and materials availability:** All data are available in the main text or the supplementary materials.

SUPPLEMENTARY MATERIALS

science.org/doi/10.1126/science.adm7034
Materials and Methods
Supplementary Text
Figs. S1 to S17
Tables S1 to S5

Submitted 1 November 2023; resubmitted 5 April 2024
Accepted 2 August 2024
10.1126/science.adm7034